



Communication

Precipitation and Soil Moisture Variation over the Tibetan Plateau to the Anomaly of Indian Summer Monsoon from 1979 to 2019

Tianyu Liu ¹, Jinghua Chen ¹, Yuanjie Zhang ¹ and Zhiqiu Gao ^{1,2,*}

¹ Key Laboratory for Aerosol-Cloud-Precipitation of China Meteorological Administration, School of Atmospheric Physics, Nanjing University of Information Science & Technology, Nanjing 210044, China; 202391000005@nuist.edu.cn (T.L.); jhchen@nuist.edu.cn (J.C.); yuanjiez@nuist.edu.cn (Y.Z.)

² State Key Laboratory of Atmospheric Boundary Layer Physics and Atmospheric Chemistry, Institute of Atmospheric Physics, Chinese Academy of Sciences, Beijing 100029, China

* Correspondence: zgao@nuist.edu.cn

Abstract: The Indian Summer Monsoon (ISM) can profoundly influence the summer precipitation patterns of the Tibetan Plateau (TP) and indirectly affect the TP's soil humidity. This study investigates the responses of TP's precipitation and soil moisture to the ISM in the monsoon season (June to September, JJAS) from 1979 to 2019. Precipitation in the TP and the ISM intensity generally exhibit a positive correlation in the west and a negative correlation in the east. The response of TP soil moisture to the ISM generally aligns with precipitation patterns, albeit with noted inconsistencies in certain TP regions. A region exhibiting these inconsistencies (30°–32°N, 80°–90°E) is selected as the study area, hereafter referred to as IRR. In periods of strong ISM, precipitation in IRR increases, yet soil moisture decreases. Conversely, in years with a weak ISM, the pattern is reversed. During strong ISM years, the rainfall increase in IRR is modest, and the soil remains drier compared to other TP regions. Under the combined effects of a marginal increase in precipitation and relatively rapid evaporation, soil moisture in the IRR decreased during years of strong ISM. During weak ISM years, the surface temperature in the IRR is higher compared to strong ISM years, potentially accelerating the melting of surface permafrost and snow in this region. Additionally, glacier meltwater, resulting from warmer temperatures in the northwest edge of the TP, may also result in the humidification of the soil in the IRR.

Keywords: the Tibetan Plateau; Indian summer monsoon; precipitation; soil moisture



Citation: Liu, T.; Chen, J.; Zhang, Y.; Gao, Z. Precipitation and Soil Moisture Variation over the Tibetan Plateau to the Anomaly of Indian Summer Monsoon from 1979 to 2019. *Remote Sens.* **2024**, *16*, 1014. <https://doi.org/10.3390/rs16061014>

Academic Editor: Yuriy Kuleshov

Received: 6 February 2024

Revised: 11 March 2024

Accepted: 11 March 2024

Published: 13 March 2024



Copyright: © 2024 by the authors. Licensee MDPI, Basel, Switzerland. This article is an open access article distributed under the terms and conditions of the Creative Commons Attribution (CC BY) license (<https://creativecommons.org/licenses/by/4.0/>).

1. Introduction

The Tibetan Plateau (TP) along with its adjacent areas, commonly considered as the 'Asian Water Tower', function as a significant water distribution system [1,2]. Given that the TP spans roughly 2.4×10^6 km² and boasts a mean altitude surpassing 4000 m, the summer 'heat pump' effect generated by the TP's heat source induces the convergence of water vapor from tropical marine areas over the TP [3,4]. Substantial quantities of water are stored on the TP in diverse forms. It contains over 3.6×10^4 glaciers [5,6] and the extent of permafrost on the TP reached approximately 0.8×10^6 km² [7]. Furthermore, the TP contains over 1200 lakes, with a total lake area exceeding 4.6×10^4 km² [8]. Meanwhile, the TP ceaselessly delivers water to almost 2 billion people in downstream areas [9,10]. Over ten great rivers have their sources in the TP [11]. Precipitation serves as a crucial link in the TP's hydrological cycle, while soil moisture functions as a key parameter in both water circulation and the balance of energy [12,13].

The TP experiences inconsistent summertime precipitation distribution, with a declining tendency from southeast to northwest [14–17]. This trend aligns with the prevalence of

atmospheric moisture in the southeastern region of the TP and a lower concentration in the northwestern areas [18]. Aside from local water vapor recycling [19], external atmospheric moisture transport, influenced by large-scale circulation, is the most important source of water vapor for rainfall over the TP [16,20,21]. Numerous prior researches have attested that the fluctuation in water vapor over the southern region of the TP is governed by the Indian Summer Monsoon (ISM) system [14,22–27]. Feng and Zhou (2012) noted that during summertime, precipitation over southeastern TP is predominantly driven by water vapor that conveyance is influenced by the ISM [14]. Zhang et al. [26] quantified the contribution of ISM water vapor transport through applying the improved Water Accounting Model. The research indicated that regions in the southeast of the TP, dominated by the ISM, contribute over 50 percent of the precipitation moisture for the southern TP. A study by Guo et al. [22] further explored the association between ISM activities and precipitation anomalies in the southeastern TP. The findings suggest that the southeastern TP precipitation from July to August shows a positive correction with the ISM persistence and its intensity. The ISM affects the distribution of summer precipitation on the TP through the transport of water vapor, and the strength and duration of the ISM will influence the amount of the TP summer precipitation.

The spatial pattern of soil moisture in summer is primarily influenced by precipitation, characterized by higher soil water content in the southwest and lower soil water content in the northeast [28–30]. However, in addition to precipitation, soil moisture on the plateau is also determined by temperature [29], evaporation [30,31], and snow melt [32–34], among other factors. The study by Bai et al. [29] pointed out that temperature regulates the soil humidity in most parts of the TP and dominates in parts of the southeastern TP. Deng et al. [30] conducted a detailed examination of how soil moisture is affected by regional climatic shifts in the hinterland of the TP and found that soil moisture in the northwest of the hinterland correlates negatively with precipitation. The soil humidity in the northwest part of the TP hinterland might be impacted by the interaction of changing amounts of rain and increased evapotranspiration. Barnett et al. [35] and Yasunari et al. [36] have pinpointed a significant impact of the snow cover, noting that melting snow can increase the land surface humidity. In general, TP soil moisture is affected by the combined influence of various factors such as precipitation, surface temperature, and vegetation cover, with precipitation being the dominant factor.

Previous studies have pointed out that the spring soil moisture in the TP will have a time-lagged effect on the Asian Summer Monsoon (ASM) [37–39]. The study by Chow et al. [37] illustrated that the increase in spring soil moisture over the TP may also weaken the Tibetan High in June and so the strength of the ASM. The result of the study by Ullah et al. [39] showed that the TP spring soil moisture negatively correlated with the ASM onset indices. Conversely, the ISM, as a subsystem of ASM, can indirectly also influence TP summer soil moisture through precipitation which needs to be further investigated. The present work attempts to explore how the precipitation and soil moisture over the TP respond to the ISM and to investigate the mechanism responsible for the inconsistencies in precipitation and soil moisture responses to the ISM from June through September, spanning 1979 to 2019.

2. Materials and Methods

This study utilizes ERA5-Land and ERA5 monthly reanalysis data, covering the period from 1979 to 2019 and specifically during the monsoon period (June to September), as developed by the ECMWF. The ERA5 reanalysis dataset is employed for the analysis of water vapor transportation to the TP. This dataset, featuring a spatial scale of 0.25° , encompasses 37 vertical layers [40]. The ERA5-Land reanalysis dataset utilizing a horizontal precision of $0.1^\circ \times 0.1^\circ$ grid is used to analyze the impact of the ISM over the thermodynamic processes of TP [41].

This study applies the 0.03° Third Pole high-resolution precipitation dataset (TPHiPr) with a temporal resolution of 1 h provided by Jiang et al. [42,43]. Firstly, the WRF sim-

ulation with high resolution is applied to downscaling the ERA5 reanalysis data from a horizontal resolution of 0.25° to 0.03° . Then they merged it with gauge data corrected by a machine learning method to generate the final TPHiPr dataset. Compared to other widely-used precipitation datasets, the TPHiPr, with its superior spatial and temporal resolution, yields more accurate descriptions of precipitation events over the TP region (25.7° – 41.3° N, 61.0° – 105.6° E) [44].

The monthly 0.25° volumetric soil moisture (VSM) data ($\text{m}^3 \text{m}^{-3}$) used in this study for the duration from 1979 to 2019 can be downloaded from the Copernicus Data Store (CDS) website [45]. This dataset estimates surface soil moisture globally through an extensive array of satellite sensors. The latest Version v202212 of the combined product was used in this study since the combined product outshone the other products in the series [28]. Compared to the previous version, version V202212 includes FengYun-3C, FengYun-3D, and ASCAT-C data for the first time, equivalent to CCI version 7. It is able to depict the latest leading edge of the soil moisture dataset derived from the satellites.

This study utilized the TP evaporation dataset on a monthly basis from 1979 to 2018 in Version 2.0, with a spatial scale of 0.1° , provided by Wang et al. [46,47]. The dataset primarily uses ERA5 net radiation data and the China Meteorological Forcing Dataset (CMFD) as inputs and is calculated using the modified sigmoid generalized complementary (SGC) evaporation. This dataset has demonstrated high efficiency and accuracy in estimating evaporation across the TP.

In order to capture the interannual fluctuations of the ISM [48], the ISM Index (IMI) was devised. The IMI, as defined by Wang et al. [49,50], has been adopted in this research. The IMI was defined on the disparity in 850 h Pa latitudinal winds within two specific regions. One is an Arabian Sea region (5° – 15° N, 40° – 80° E), and the other is an area that encompasses part of the eastern part of the TP (20° – 30° N, 70° – 90° E). Compared to the All-India Summer Rainfall Index, traditionally used as an indicator for the ISM, the IMI presents a more comprehensive view. Specifically, it not only indicates large-scale circulation anomalies but also incorporates regional rainfall anomalies, encompassing areas including the Bay of Bengal, India, and the eastern Arabian Sea.

The 41 years of IMI data from June to September (JJAS) for the duration of 1979–2019 were retrieved from the Monsoon Monitoring Page. During the computation process, the IMI have been standardized using Z-score normalization. The top 20% of the IMI indicates strong ISM years, while the bottom 20% signifies weak ISM years. Thus, eight strong ISM years are selected as 1980, 1983, 1988, 1994, 1996, 1998, 2005, and 2006 and eight weak ISM years are 1979, 1987, 1997, 2009, 2012, 2014, 2015, and 2018 (Table 1). The remaining 41 years are normal ISM years, except for the selected strong and weak ISM years.

Table 1. Classification based on the IMI. The top 20% of the IMI from 1979 to 2019 indicates strong ISM years, while the bottom 20% signifies weak ISM years.

Strong ISM Years	Weak ISM Years
1980	1979
1983	1987
1988	1997
1994	2009
1996	2012
1998	2014
2005	2015
2006	2018

The integrated water transport (IVT) metric is employed to represent an integral of the total amount of water vapor in a whole layer [51,52]. The IVT can be calculated as in Equation (1).

$$IVT \left(\text{kg m}^{-1} \text{s}^{-1} \right) = -\frac{1}{g} \int_{P_{sfc}}^{P_{top}} q \vec{V} dp \quad (1)$$

where g is the gravitational acceleration (m s^{-2}), P_{sfc} is the pressure of the surface (hPa), P_{top} is the top of the atmosphere, setting at 100 hPa; \vec{V} is the wind velocity (m s^{-1}), and q is the specific humidity (kg kg^{-1}).

The location and topography of the study region, the TP, are shown in Figure 1.

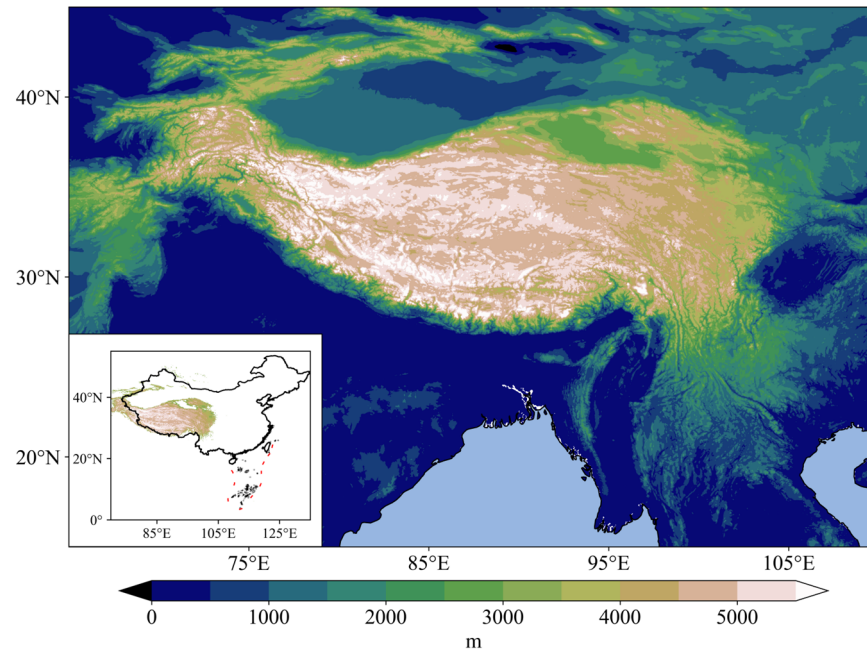


Figure 1. The location and topography of the Tibetan Plateau (TP) region.

3. Results

3.1. Characteristics of Precipitation and Soil Moisture over the TP during Normal ISM Years

Precipitation across the TP exhibits an uneven distribution, both temporally and spatially. Regarding temporal distribution, precipitation on the TP predominantly occurs in summer, contributing to over 60% of the annual total [53]. Spatially, the rainfall frequency and amount are greater in the southeastern than in the northwestern TP [54]. As shown in Figure 2, precipitation over the TP declines from southeast to northwest during JJAS in normal ISM years. Large-scale circulation-driven external water vapor transport significantly contributes to the spatial heterogeneity of TP summer precipitation. The monthly averaged spatial distribution of IVT over the TP and its adjacent regions in JJAS of normal ISM years is demonstrated in Figure 3. A cyclonic circulation pattern is present in the northern part of the Indian Peninsula. The southwest airflow originating from the Arabian Sea, after passing through the northern Bay of Bengal (BOB), carries a substantial amount of moisture northward. Part of it turns westward by the cyclonic system, transporting warm and moist airflow into the southwestern TP. Another portion of the airflow moves directly northward, entering the southeastern region of the TP via the Yarlung Tsangpo Grand Canyon, serving as a natural moisture channel. Additionally, the mid-latitude westerlies serve as a vapor transfer channel, driving moisture to the southwestern part of the TP.

Figure 4 presents the distribution of correlation coefficients between the ISM and precipitation over the TP and its adjacent areas in JJAS from 1979 to 2019. As per Figure 4, the ISM has a significant influence on the precipitation over most of the TP in summer. Specifically, the distribution of the positive correlation coefficient is in the western part of the TP. The rainfall of the eastern region of the TP correlates negatively with the ISM. In parts of the southwestern, southeastern, and northeastern TP, the correlation coefficient passed the 95% significance test. The present study further performed correlation analyses of the IMI with precipitation over the TP and its adjacent areas in the early (JJ), middle (JA), and late (AS) monsoon periods from 1979 to 2019. The ISM showed a more significant positive correlation with precipitation in the southwestern part of the TP and a more

significant negative correlation with precipitation in the northwestern part of the TP during the early (JJ) monsoon period compared with the whole (JJAS) monsoon period. Figure 5 illustrates that, during strong ISM years, in the southwestern region of the TP, close to the southern slopes, there was an approximate 40 mm rise in precipitation, but there was a notable decrease in rainfall in the southeastern section of the TP compared to weak ISM years. Figure 6 demonstrates the distribution pattern of correlation coefficients between the ISM and IVT over the TP and its adjacent areas. In conjunction with Figure 3, it indicates that the ISM positively affects the southwestward and southward moisture transport from the BOB and has a negative impact on the southeastward water vapor transport from the Arabian Sea. During active ISM phases, water vapor transport from the BOB would be promoted by the south-easterly jet, reaching the southwestern TP and potentially contributing moisture to the increased precipitation in the western TP. When the ISM is inactive, water vapor transportation originating from the Arabian Sea intensifies, conveying more moisture to the TP eastern section. This is consistent with the findings of previous research [55,56].

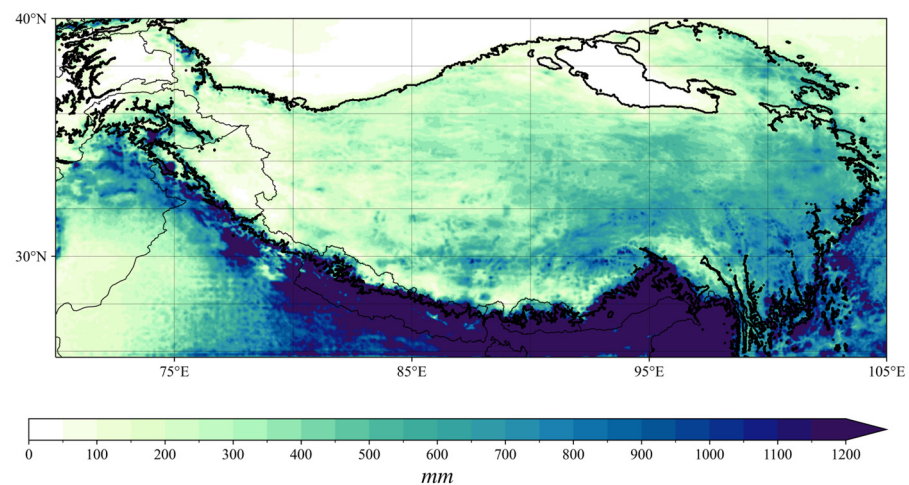


Figure 2. The spatial patterns of precipitation (units: mm) over the TP and its adjacent areas in JJAS of normal ISM years. The bold black lines denote the elevation of 3000 m.

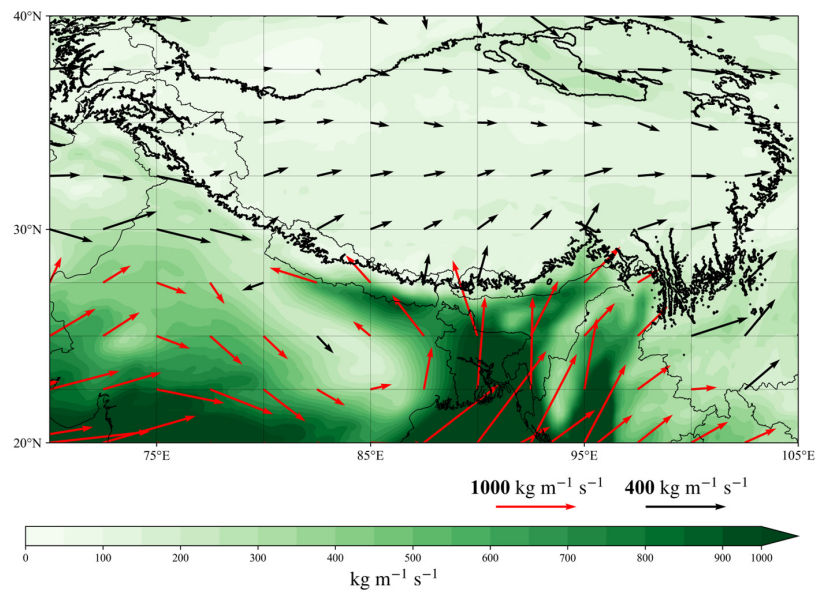


Figure 3. The spatial patterns of IVT (units: $\text{kg m}^{-1} \text{s}^{-1}$) over the TP and its adjacent areas in JJAS of normal ISM years. The bold black lines denote the elevation of 3000 m. The IVT of more than $300 \text{ kg m}^{-1} \text{s}^{-1}$ is shown by the red arrow and the IVT of less than $300 \text{ kg m}^{-1} \text{s}^{-1}$ is shown by the black arrow.

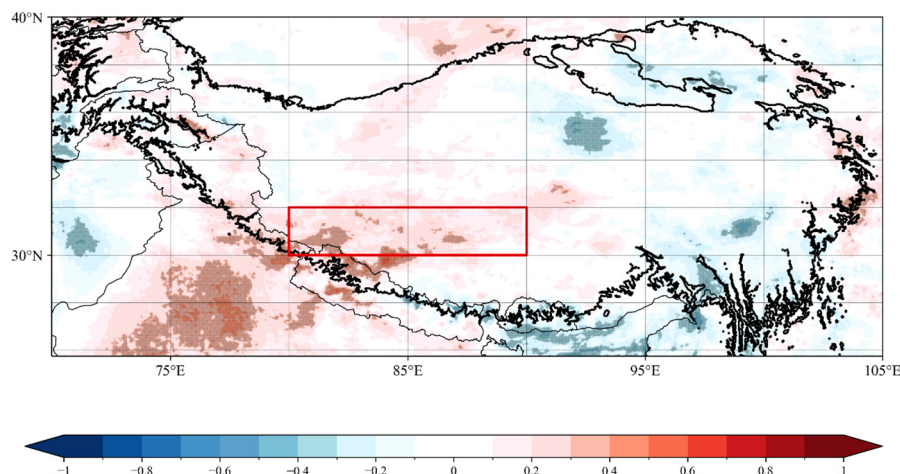


Figure 4. The distribution of correlation coefficients between the ISM and precipitation over the TP and its adjacent areas in JJAS from 1979 to 2019. Dotted areas indicate significant trends at the 95% confidence level based on the Pearson Test. The bold black lines denote the elevation of 3000 m. The box in red solid lines represents the position of the IRR (30° – 32° N, 80° – 90° E).

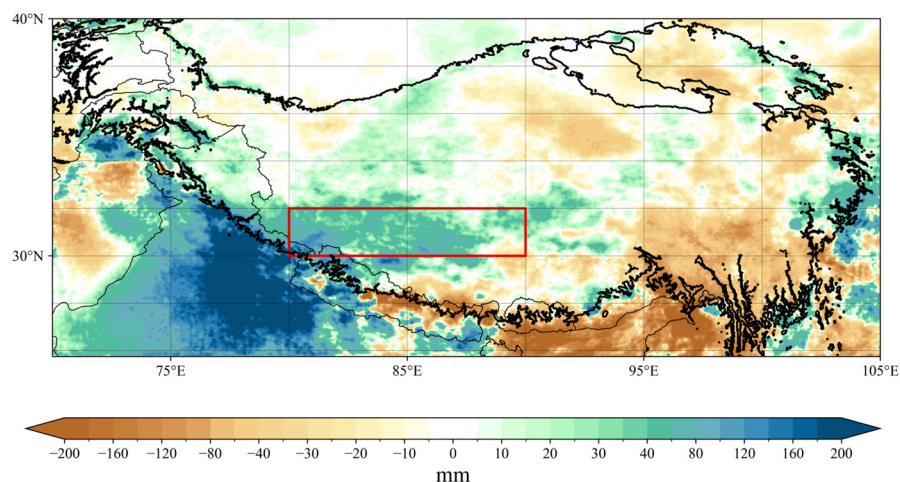


Figure 5. The spatial patterns of precipitation anomalies over the TP and its adjacent areas in JJAS (strong ISM years values minus weak ISM years values, units: mm). The bold black lines denote the elevation of 3000 m. The box in red solid lines represents the position of the IRR (30° – 32° N, 80° – 90° E).

The monthly averaged spatial distribution of soil moisture on the TP, as depicted in Figure 7, shows a declining trend from east to west. The Himalayas intercept a significant amount of water vapor, leading to precipitation [18]. Consequently, a belt of high soil moisture forms along the front of the TP southern slope. Figure 8 demonstrates the distribution of correlation coefficients between the ISM and volumetric soil moisture over the TP and its adjacent areas in JJAS from 1979 to 2019. Comparing Figures 4 and 8, the response of TP soil moisture to the ISM is generally consistent with that of precipitation. In the majority of areas in the eastern TP, the correlation coefficient exhibits negative values. The positive correlation coefficient is mainly located 30° N south of the TP and northwestern part of the TP. Nevertheless, in parts of the southwestern part of the TP, the precipitation shows a positive correlation to the ISM, and the soil moisture shows a negative correlation. A region exhibiting inconsistent responses of precipitation and soil moisture to the ISM, defined as (30° – 32° N, 80° – 90° E) is selected as the study area, referred to as IRR. Essentially, during periods of strong ISM, precipitation in the IRR increases, while soil moisture decreases. The situation is reversed in weak ISM years.

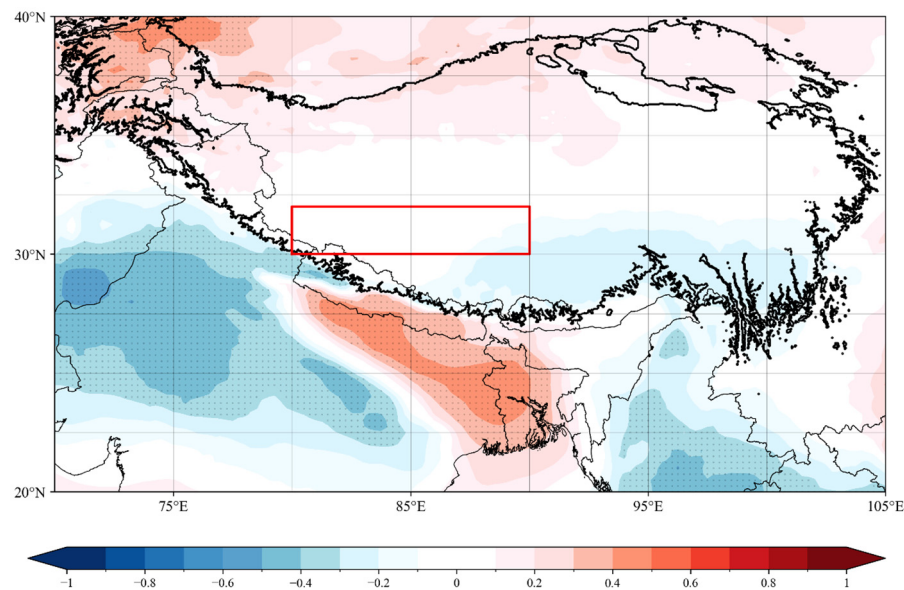


Figure 6. The distribution of correlation coefficients between the ISM and IVT over the TP and its adjacent areas in JJAS from 1979 to 2019. Dotted areas indicate significant trends at the 95% confidence level based on the Pearson Test. The bold black lines denote the elevation of 3000 m. The box in red solid lines represents the position of the IRR (30°–32°N, 80°–90°E).

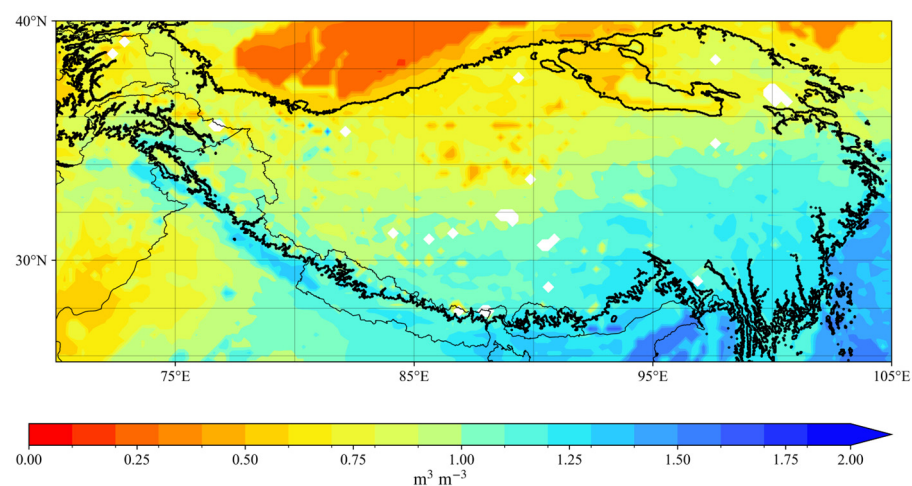


Figure 7. The spatial patterns of volumetric soil moisture (units: $\text{m}^3 \text{m}^{-3}$) over the TP and its adjacent areas in JJAS of normal ISM years. The bold black lines denote the elevation of 3000 m.

3.2. Response of Soil Moisture to the Precipitation in IRR during Strong ISM Years

As illustrated by Figure 9, when the ISM is strong, soil moisture in the IRR decreases. Figure 10 demonstrates that more evaporation occurs in the IRR during strong ISM years compared to weak ISM years. Soil evaporation consumes a large amount of latent heat, so latent heat flux in the IRR is smaller in strong ISM years than in weak years (Figure 11). The relatively small IVT anomalies between strong and weak ISM years in IRR (Figure 12) denote that the impact of external moisture transportation on the IRR is comparatively minimal. Local evaporation contributes more to precipitation in the IRR. The majority of evaporation is recycled within the IRR, and the rest may be transported outside [57]. Even though precipitation increased in the IRR during strong ISM years (Figure 5), the rainfall amount in the southwestern part of the TP is relatively lighter and the soil moisture content is lower than that in other areas of the TP. Notably, an increase in precipitation does not invariably result in heightened soil moisture. Under the combined effects of insignificant precipitation increase and relatively rapid evaporation, soil moisture in IRR decreased in

strong ISM years. This aligns with Meng et al.'s (2017) [31] findings, which suggest that minor reductions in soil moisture in the TP's western and northern parts could stem from rapid evaporation and modest rainfall alterations. Deng et al. (2020) [30] also reached a similar conclusion in their study on the response of soil moisture to climate change over the Three River Region (TRSR) on the TP. The soil moisture in the northwest TRSR is not consistent with the precipitation, due to relatively small changes in precipitation and increased evapotranspiration.

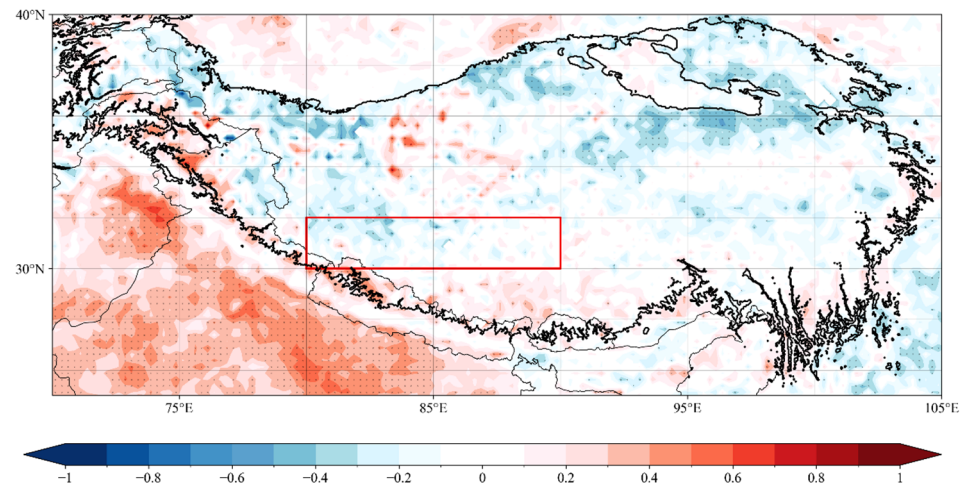


Figure 8. The distribution of correlation coefficients between the ISM and volumetric soil moisture over the TP and its adjacent areas in JJAS from 1979 to 2019. Dotted areas indicate significant trends at the 95% confidence level based on the Pearson Test. The bold black lines denote the elevation of 3000 m. The box in red solid lines represents the position of the IRR (30°–32°N, 80°–90°E).

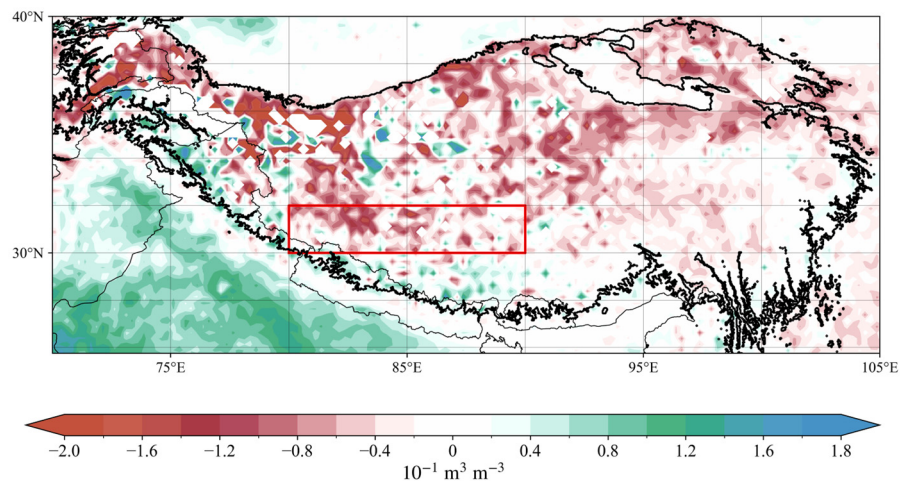


Figure 9. The spatial patterns of volumetric soil moisture anomalies over the TP and its adjacent areas during JJAS (strong ISM years values minus weak ISM years values, units: $10^{-1} \text{ m}^3 \text{ m}^{-3}$). The bold black lines denote the elevation of 3000 m. The box in red solid lines represents the position of the IRR (30°–32°N, 80°–90°E).

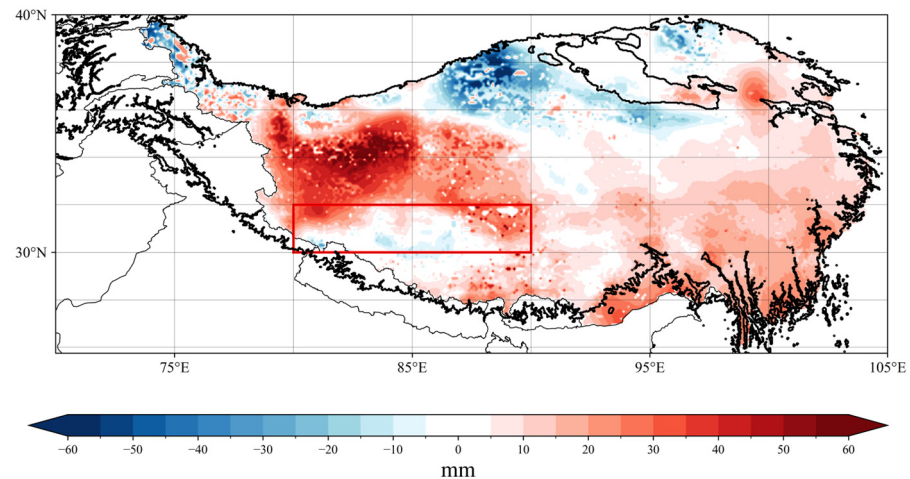


Figure 10. The spatial patterns of evaporation anomalies over the TP and its adjacent areas during JJAS (strong ISM years values minus weak ISM years values, units: mm). The topographic elevation of 3000 m is marked by bold black lines. The box in red solid lines represents the position of the IRR (30°–32°N, 80°–90°E).

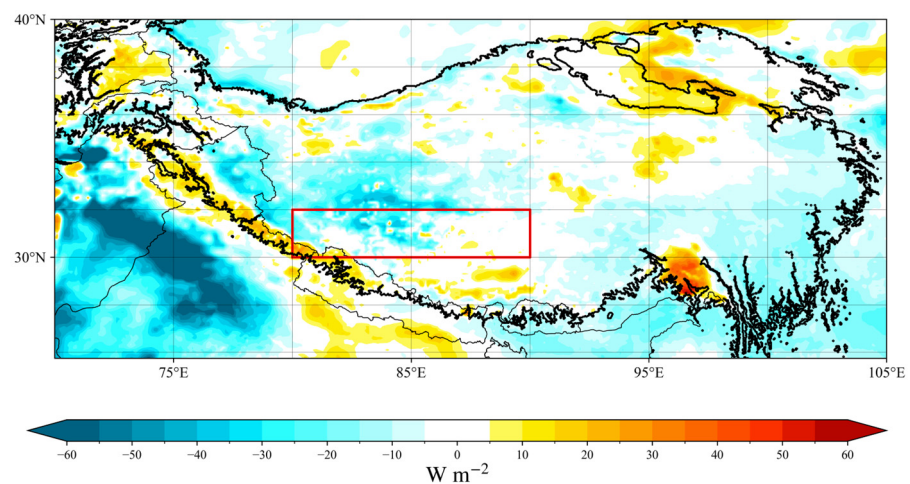


Figure 11. The spatial patterns of surface latent heat flux anomalies over the TP and its adjacent areas during JJAS (strong ISM years values minus weak ISM years values, units: $W m^{-2}$). The topographic elevation of 3000 m is marked by bold black lines. The box in red solid lines represents the position of the IRR (30°–32°N, 80°–90°E).

3.3. Response of Soil Moisture to the Precipitation in IRR during Weak ISM Years

Surface temperatures in IRR are higher during weak ISM years compared to strong ISM years, as is exhibited in Figure 13. Since IRR is located in the west-central part of the TP, the snowmelt period in this region is later and lasts longer compared to other regions [58]. The results of previous studies indicate that permafrost thawing in the area where IRR is located begins around June to July [59,60]. Elevated surface temperatures can lead to the melting of snow and surface frozen soil, the infiltration of snowmelt water subsequently causing an enhancement in IRR soil humidity [61–63]. Furthermore, surface temperatures in the northwest of the plateau have also increased during weak ISM years. Considering the presence of numerous temperate glaciers in the northwestern corner of the TP, including the Baltoro and Kondus Glaciers [64,65], the increase in surface temperature in that region may accelerate glacier melting. Present studies have suggested that glacial meltwater is one of the factors that increase soil moisture content in downstream regions [66,67]. The flow of glacier meltwater into the IRR, located in the downstream region, would also lead to an increase in soil moisture in the IRR. In conclusion, the rising soil moisture of the

IRR during weak ISM years is likely related to the melting of snow or surface permafrost, coupled with the significant rise in IRR surface temperature. Additionally, glacial meltwater resulting from rising surface temperatures in the northwestern corner of the TP is also a likely contributing factor.

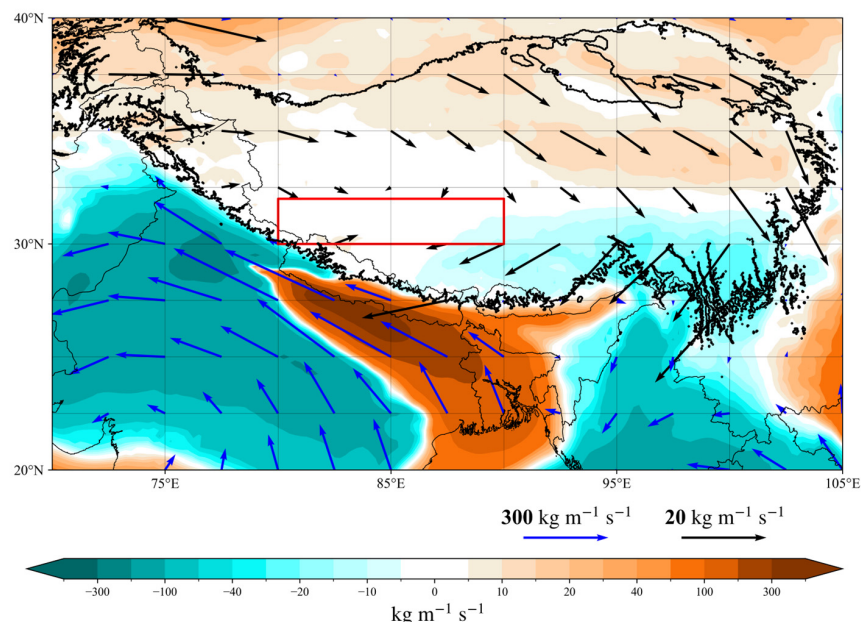


Figure 12. The spatial patterns of IVT anomalies over the TP and its adjacent areas during JJAS (strong ISM years values minus weak ISM years values, units: $\text{kg m}^{-1} \text{s}^{-1}$). The IVT inside the TP is marked by the black arrow and that outside the TP is marked by the blue arrow. The topographic elevation of 3000 m is marked by bold black lines. The box in red solid lines represents the IRR (30° – 32° N, 80° – 90° E).

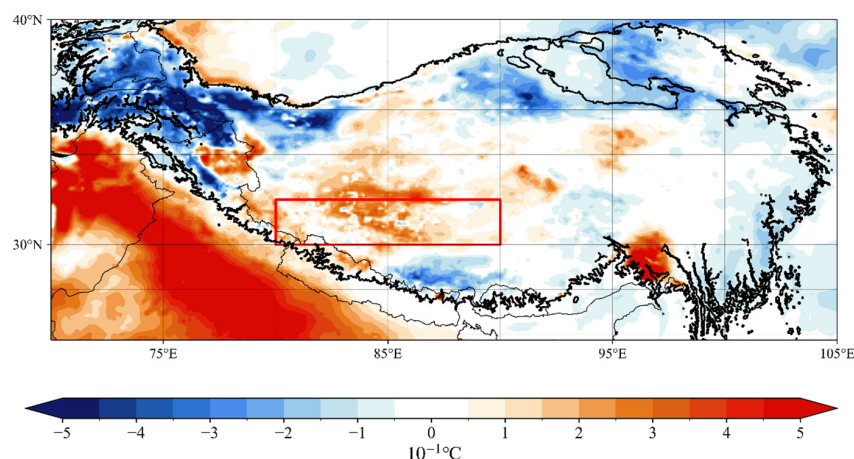


Figure 13. The spatial patterns of surface temperature anomalies over the TP and its adjacent areas during JJAS (weak ISM years values minus strong ISM years values, units: $10^{-1} \text{ }^{\circ}\text{C}$). The topographic elevation of 3000 m is marked by bold black lines. The position of the IRR (30° – 32° N, 80° – 90° E) is highlighted in red boxes.

4. Discussion

4.1. Relationship between TP Soil Moisture, Precipitation, Temperature, and Other Factors

The result of this study demonstrated that the response of TP soil moisture to the ISM generally aligns with precipitation patterns, albeit with noted inconsistencies in IRR. Even though previous studies have illustrated that precipitation is the dominant factor affecting soil moisture in much of the TP regions [68,69], it is not the only factor that increases soil

moisture. Temperature can influence TP soil moisture in two ways [29]. The increased temperatures will result in increased evaporation and reduce the humidity of the soil. On another hand, the increased temperatures can also promote the process of snowmelt and increase soil moisture. Due to the complex topography of the TP, snow-cover situations in TP are also complicated. Snow cover datasets over the TP have overestimations because of cloud coverage [70,71]. In view of the TP, water cycle processes are complex. It is difficult to quantify the contribution of the melting of snow and glaciers to the variability of soil moisture based on the present data. In future work, some issues still deserve further analysis. For example, quantifying the contribution of the melting of snow and glaciers to the variability of soil moisture to better understand the mechanism of soil moisture and precipitation under the influence of the ISM.

This study primarily concentrates on the effects of evaporation and surface temperature on the inconsistent responses of IRR precipitation and soil humidity to the ISM. Additional factors also influence soil moisture. For instance, prior research indicates that soil moisture irregularities arising in the spring on the TP might be retained in the deep layers, maintaining their presence for as long as a month into the summer [72]. Therefore, the summer soil moisture over the TP will also be affected by the spring precipitation pattern. The cause of enhanced evaporation in the IRR region during strong ISM years remains a matter of interest. Soil moisture may also be affected by other factors like wind speed. Under a certain threshold, as the wind speed increases, the evaporation rate increases [73]. Future studies could further examine the increased evaporation in the IRR during strong ISM years, especially if datasets featuring maximum or extreme wind speeds with high spatiotemporal resolution become available, considering that the current ERA5 wind speed data are average values.

In addition, this study chose IRR as the study region since the precipitation and soil moisture in IRR showed different responses to the ISM which is relatively less significant in other regions of the TP. However, other areas of the TP are also worthy of investigation which will be focused on in further studies. This study also performed correlation analyses of the IMI with precipitation over the TP and its adjacent areas in the early (JJ), middle (JA), and late (AS) monsoon periods from 1979 to 2019. The results show that the correlation between the ISM and TP precipitation is relatively significant during the early (JJ) monsoon season and the correlation decreases during the late (AS) monsoon period. More attention could be paid to the early (JJ) monsoon period in future studies of the ISM and TP precipitation.

4.2. Data Uncertainties

Moreover, the accuracy of the data utilized can significantly impact the results. The satellite-based soil moisture dataset provided by Copernicus Climate Data Store has many versions in the past, such as Version 201912 [74] and Version 202012 [75]. Different versions of the dataset may lead to differences in the results. The latest Version 202212, which updates data from FengYun-3C, FengYun-3D, and ASCAT-C for the first time, depicts the latest leading edge of the soil moisture dataset derived from the satellites. Consequently, the version of the satellite-based soil moisture dataset employed in this study is Version 202212. Considering the special and complex topography of the TP, there will certainly be uncertainties in the data. Factors such as soil type, soil composition, and types of vegetation cover all affect the accuracy of satellite-derived soil moisture products [76,77]. The study by Wang et al. [78] illustrated that Fengyun satellite soil moisture products tend to overestimate the in-situ measurements, particularly following precipitation events and during periods of vegetation growth when comparing Fengyun satellite soil data with actual measurements from the Naqu region of the TP. However, it aligns with the general trend of the observation data. This could potentially be attributed to the fact that the X-band, employed by the Fengyun Satellite for detection purposes, possesses a limited penetration depth, with its findings being considerably impacted by surface vegetation [79]. If datasets with higher temporal or spatial resolution or longer time series are available in the future, the result of this study can be verified.

5. Conclusions

This work examined the responses of TP precipitation and soil moisture to the ISM in the monsoon season (June to September) between 1979 and 2019. The analysis is grounded in soil moisture gridded data obtained from satellite remote sensing [49], the TPHiPr dataset, and ERA5 reanalysis data. TP precipitation generally exhibits a positive correlation with the ISM intensity in the west and a negative correlation in the east. Considering that precipitation is the dominant factor affecting soil moisture in much of the TP regions, the ISM can indirectly influence soil moisture through precipitation. The response of soil moisture of the TP to the ISM is roughly consistent with that of precipitation. In the majority of areas of the eastern TP, soil moisture shows a negative correlation with the ISM. A positive correlation coefficient between soil moisture and the ISM is primarily observed south of 30°N on the TP and in its northwestern part. However, there is a region with inconsistent responses of precipitation and soil moisture to the ISM (30°–32°N, 80°–90°E), referred to as IRR.

During periods of active ISM influence, an increase in precipitation within the IRR is accompanied by increased evaporation. However, the rainfall in the southwestern TP is comparatively lower, and the soil moisture content is lower than in other regions of the TP. TP soil moisture was influenced by both precipitation and evaporation. The balance between these two factors is critical in determining the overall impact on soil moisture. Under the combined effects of insignificant precipitation increase and relatively rapid evaporation, soil moisture in IRR decreased in strong ISM years. What is more, this study found that the impact of external moisture transportation dominated by the ISM on the IRR is comparatively minimal. Local evaporation contributes more to precipitation in the IRR. The majority of evaporation is recycled within the IRR, and the rest may be transported outside. This mechanism may consume some of the water vapor in the IRR region. In weak ISM years, the surface temperature in IRR is higher than in strong ISM years, potentially accelerating the melting of surface permafrost and snow in this area. Additionally, in the northwest corner of the TP, a region with a majority of temperate glaciers, the surface temperature rose during weak ISM years. The melting glaciers may also contribute to increased soil moisture in the IRR during weak ISM years. Consequently, soil moisture in the IRR rises even during weak ISM years when precipitation decreases.

Author Contributions: Conceptualization, Z.G.; methodology, Z.G. and J.C.; software, T.L.; formal analysis, T.L. and Y.Z.; data curation, T.L.; investigation, T.L.; writing—original draft preparation, T.L.; writing—review and editing, Z.G. and J.C. All authors have read and agreed to the published version of the manuscript.

Funding: This research was funded by the Second Tibetan Plateau Scientific Expedition and Research Program (Grant 2019QZKK0102), the Tibetan Plateau Scientific Expedition and Research (STEP) program (Grant 2019QZKK0105), the National Science Foundation of China (42075067), and the Qinghai Science and Technology Department Project (Grant 2020-ZJ-711).

Data Availability Statement: The ERA5-Land and ERA5 monthly reanalysis data is downloaded from the CDS (<https://climate.copernicus.eu/climate-reanalysis>) (accessed on 20 September 2023). The Third Pole high-resolution precipitation dataset (TPHiPr) is downloaded from the National Tibetan Plateau/Third Pole Environment Data Center (<https://cstr.cn/18406.11.Atmos.tpd.272763>) (accessed on 25 September 2023). The evaporation dataset of the Tibetan Plateau at the monthly scale (1979–2018) V2.0. is downloaded from the National Tibetan Plateau/Third Pole Environment Data Center (<https://cstr.cn/18406.11.Meteoro.tpd.271585>) (accessed on 25 October 2023). The soil moisture gridded data from 1978 to present v202212 is downloaded from Copernicus Climate Change Service (C3S) CDS (<https://cds.climate.copernicus.eu/cdsapp#!/dataset/satellite-soil-moisture?tab=overview>) (accessed on 31 October 2023). The IMI is accessible on the Monsoon Monitoring Page (<http://apdr. soest.hawaii.edu/projects/monsoon/seasonal-monidx.html>) (accessed on 15 August 2023).

Conflicts of Interest: The authors declare no conflicts of interest.

References

1. Xu, X.; Lu, C.; Shi, X.; Gao, S. World Water Tower: An Atmospheric Perspective. *Geophys. Res. Lett.* **2008**, *35*, 2008GL035867. [[CrossRef](#)]
2. Yao, T.; Bolch, T.; Chen, D.; Gao, J.; Immerzeel, W.; Piao, S.; Su, F.; Thompson, L.; Wada, Y.; Wang, L.; et al. The Imbalance of the Asian Water Tower. *Nat. Rev. Earth Env.* **2022**, *3*, 618–632. [[CrossRef](#)]
3. Wu, G.; Liu, Y. Impacts of the Tibetan Plateau on Asian Climate. *Meteorol. Monogr.* **2016**, *56*, 7.1–7.29. [[CrossRef](#)]
4. Li, J.; Deng, M.; Wang, X.; Wang, X.; Ma, R. Clustering and Analysis of Air Source Heat Pump Air Heater Usage Patterns of Inhabitants in Qinghai-Tibet Plateau Areas. *J. Build. Eng.* **2023**, *68*, 106149. [[CrossRef](#)]
5. Yao, T.; Thompson, L.G.; Mosbrugger, V.; Zhang, F.; Ma, Y.; Luo, T.; Xu, B.; Yang, X.; Joswiak, D.R.; Wang, W.; et al. Third Pole Environment (TPE). *Environ. Dev.* **2012**, *3*, 52–64. [[CrossRef](#)]
6. Kang, S.; Xu, Y.; You, Q.; Flügel, W.-A.; Pepin, N.; Yao, T. Review of Climate and Cryospheric Change in the Tibetan Plateau. *Environ. Res. Lett.* **2010**, *5*, 015101. [[CrossRef](#)]
7. Jin, H.; Jin, X.; He, R.; Luo, D.; Chang, X.; Wang, S.; Marchenko, S.S.; Yang, S.; Yi, C.; Li, S.; et al. Evolution of Permafrost in China during the Last 20 Ka. *Sci. China Earth Sci.* **2019**, *62*, 1207–1223. [[CrossRef](#)]
8. Wang, L.; Zhao, L.; Zhou, H.; Liu, S.; Du, E.; Zou, D.; Liu, G.; Xiao, Y.; Hu, G.; Wang, C.; et al. Contribution of Ground Ice Melting to the Expansion of Selin Co (Lake) on the Tibetan Plateau. *Cryosphere* **2022**, *16*, 2745–2767. [[CrossRef](#)]
9. Li, L.; He, C.; Li, J.; Zhang, J.; Li, J. The Supply and Demand of Water-Related Ecosystem Services in the Asian Water Tower and Its Downstream Area. *Sci. Total Environ.* **2023**, *887*, 164205. [[CrossRef](#)] [[PubMed](#)]
10. Immerzeel, W.W.; Lutz, A.F.; Andrade, M.; Bahl, A.; Biemans, H.; Bolch, T.; Hyde, S.; Brumby, S.; Davies, B.J.; Elmore, A.C.; et al. Importance and Vulnerability of the World's Water Towers. *Nature* **2020**, *577*, 364–369. [[CrossRef](#)]
11. Li, S.-L.; Yue, F.-J.; Liu, C.-Q.; Ding, H.; Zhao, Z.-Q.; Li, X. The O and H Isotope Characteristics of Water from Major Rivers in China. *Chin. J. Geochem.* **2015**, *34*, 28–37. [[CrossRef](#)]
12. Wang, L.; Wang, J.; Li, M.; Wang, L.; Li, X.; Zhu, L. Response of Terrestrial Water Storage and Its Change to Climate Change in the Endorheic Tibetan Plateau. *J. Hydrol.* **2022**, *612*, 128231. [[CrossRef](#)]
13. Yang, C.; Ma, Y.; Yuan, Y. Terrestrial and Atmospheric Controls on Surface Energy Partitioning and Evaporative Fraction Regimes Over the Tibetan Plateau in the Growing Season. *JGR Atmos.* **2021**, *126*, e2021JD035011. [[CrossRef](#)]
14. Feng, L.; Zhou, T. Water Vapor Transport for Summer Precipitation over the Tibetan Plateau: Multidata Set Analysis. *J. Geophys. Res.* **2012**, *117*, 2011JD017012. [[CrossRef](#)]
15. Ma, Y.; Tang, G.; Long, D.; Yong, B.; Zhong, L.; Wan, W.; Hong, Y. Similarity and Error Intercomparison of the GPM and Its Predecessor-TRMM Multisatellite Precipitation Analysis Using the Best Available Hourly Gauge Network over the Tibetan Plateau. *Remote Sens.* **2016**, *8*, 569. [[CrossRef](#)]
16. Wang, Z.; Duan, A.; Yang, S.; Ullah, K. Atmospheric Moisture Budget and Its Regulation on the Variability of Summer Precipitation over the Tibetan Plateau. *JGR Atmos.* **2017**, *122*, 614–630. [[CrossRef](#)]
17. Tong, K.; Su, F.; Yang, D.; Zhang, L.; Hao, Z. Tibetan Plateau Precipitation as Depicted by Gauge Observations, Reanalyses and Satellite Retrievals. *Int. J. Climatol.* **2014**, *34*, 265–285. [[CrossRef](#)]
18. Lu, N.; Qin, J.; Gao, Y.; Yang, K.; Trenberth, K.E.; Gehne, M.; Zhu, Y. Trends and Variability in Atmospheric Precipitable Water over the Tibetan Plateau for 2000–2010: PW TREND TP. *Int. J. Climatol.* **2015**, *35*, 1394–1404. [[CrossRef](#)]
19. Curio, J.; Maussion, F.; Scherer, D. A 12-Year High-Resolution Climatology of Atmospheric Water Transport over the Tibetan Plateau. *Earth Syst. Dynam.* **2015**, *6*, 109–124. [[CrossRef](#)]
20. Gao, Y.; Cuo, L.; Zhang, Y. Changes in Moisture Flux over the Tibetan Plateau during 1979–2011 and Possible Mechanisms. *J. Clim.* **2014**, *27*, 1876–1893. [[CrossRef](#)]
21. Bothe, O.; Fraedrich, K.; Zhu, X. Tibetan Plateau Summer Precipitation: Covariability with Circulation Indices. *Theor. Appl. Clim.* **2012**, *108*, 293–300. [[CrossRef](#)]
22. Guo, X.; Tian, L.; Wang, L.; Wang, Y.; Zhou, J. Controls of the Recent Precipitation Anomalies in the Southeastern Tibetan Plateau: From the Perspective of Indian Summer Monsoon Activities and Moisture Sources. *Clim. Dyn.* **2023**, *62*, 399–412. [[CrossRef](#)]
23. Chen, B.; Zhang, W.; Yang, S.; Xu, X. Identifying and Contrasting the Sources of the Water Vapor Reaching the Subregions of the Tibetan Plateau during the Wet Season. *Clim. Dyn.* **2019**, *53*, 6891–6907. [[CrossRef](#)]
24. Chen, B.; Xu, X.-D.; Yang, S.; Zhang, W. On the Origin and Destination of Atmospheric Moisture and Air Mass over the Tibetan Plateau. *Theor. Appl. Clim.* **2012**, *110*, 423–435. [[CrossRef](#)]
25. Tian, L.; Masson-Delmotte, V.; Stievenard, M.; Yao, T.; Jouzel, J. Tibetan Plateau Summer Monsoon Northward Extent Revealed by Measurements of Water Stable Isotopes. *J. Geophys. Res.* **2001**, *106*, 28081–28088. [[CrossRef](#)]
26. Zhang, C.; Tang, Q.; Chen, D.; Van Der Ent, R.J.; Liu, X.; Li, W.; Haile, G.G. Moisture Source Changes Contributed to Different Precipitation Changes over the Northern and Southern Tibetan Plateau. *J. Hydrometeorol.* **2019**, *20*, 217–229. [[CrossRef](#)]
27. Yao, T.; Masson-Delmotte, V.; Gao, J.; Yu, W.; Yang, X.; Risi, C.; Sturm, C.; Werner, M.; Zhao, H.; He, Y.; et al. A Review of Climatic Controls on $\delta^{18}\text{O}$ in Precipitation over the Tibetan Plateau: Observations and Simulations. *Rev. Geophys.* **2013**, *51*, 525–548. [[CrossRef](#)]
28. Cheng, M.; Zhong, L.; Ma, Y.; Zou, M.; Ge, N.; Wang, X.; Hu, Y. A Study on the Assessment of Multi-Source Satellite Soil Moisture Products and Reanalysis Data for the Tibetan Plateau. *Remote Sens.* **2019**, *11*, 1196. [[CrossRef](#)]
29. Bai, W.; Chen, X.; Tang, Y.; He, Y.; Zheng, Y. Temporal and Spatial Changes of Soil Moisture and Its Response to Temperature and Precipitation over the Tibetan Plateau. *Hydrol. Sci. J.* **2019**, *64*, 1370–1384. [[CrossRef](#)]

30. Deng, M.; Meng, X.; Li, Z.; Lyv, Y.; Lei, H.; Zhao, L.; Zhao, S.; Ge, J.; Jing, H. Responses of Soil Moisture to Regional Climate Change over the Three Rivers Source Region on the Tibetan Plateau. *Int. J. Climatol.* **2020**, *40*, 2403–2417. [[CrossRef](#)]
31. Meng, X.; Li, R.; Luan, L.; Lyu, S.; Zhang, T.; Ao, Y.; Han, B.; Zhao, L.; Ma, Y. Detecting Hydrological Consistency between Soil Moisture and Precipitation and Changes of Soil Moisture in Summer over the Tibetan Plateau. *Clim. Dyn.* **2018**, *51*, 4157–4168. [[CrossRef](#)]
32. Lieting, C.; Renguang, W. Interannual and Decadal Variations of Snow Cover over Qinghai-Xizang Plateau and Their Relationships to Summer Monsoon Rainfall in China. *Adv. Atmos. Sci.* **2000**, *17*, 18–30. [[CrossRef](#)]
33. Yang, K.; Wang, C. Seasonal Persistence of Soil Moisture Anomalies Related to Freeze–Thaw over the Tibetan Plateau and Prediction Signal of Summer Precipitation in Eastern China. *Clim. Dyn.* **2019**, *53*, 2411–2424. [[CrossRef](#)]
34. Yang, M.; Yao, T.; Gou, X.; Koike, T.; He, Y. The Soil Moisture Distribution, Thawing–Freezing Processes and Their Effects on the Seasonal Transition on the Qinghai–Xizang (Tibetan) Plateau. *J. Asian Earth Sci.* **2003**, *21*, 457–465. [[CrossRef](#)]
35. Barnett, T.P.; Dümenil, L.; Schlese, U.; Roeckner, E. The Effect of Eurasian Snow Cover on Global Climate. *Science* **1988**, *239*, 504–507. [[CrossRef](#)]
36. Yasunari, T.; Kitoh, A.; Tokioka, T. Local and Remote Responses to Excessive Snow Mass over Eurasia Appearing in the Northern Spring and Summer Climate. *J. Meteorol. Soc. Jpn. Ser. II* **1991**, *69*, 473–487. [[CrossRef](#)]
37. Chow, K.C.; Chan, J.C.L.; Shi, X.; Liu, Y.; Ding, Y. Time-Lagged Effects of Spring Tibetan Plateau Soil Moisture on the Monsoon over China in Early Summer. *Int. J. Climatol.* **2007**, *28*, 55–67. [[CrossRef](#)]
38. Wang, C.; Yang, K.; Zhang, F. Impacts of Soil Freeze–Thaw Process and Snow Melting Over Tibetan Plateau on Asian Summer Monsoon System: A Review and Perspective. *Front. Earth Sci.* **2020**, *8*, 133. [[CrossRef](#)]
39. Ullah, W.; Wang, G.; Lou, D.; Gao, Z.; Zhu, C.; Bhatti, A.S.; Hagan, D.F.T.; Li, S.; Jiang, T.; Su, B.; et al. The Empirical Influence of Tibetan Plateau Spring Soil Moisture on South Asian Monsoon Onset: A Linear Diagnostic Perspective. *J. Clim.* **2023**, *36*, 8723–8742. [[CrossRef](#)]
40. Hersbach, H.; Bell, B.; Berrisford, P.; Hirahara, S.; Horányi, A.; Muñoz-Sabater, J.; Nicolas, J.; Peubey, C.; Radu, R.; Schepers, D.; et al. The ERA5 Global Reanalysis. *Q. J. R. Meteorol. Soc.* **2020**, *146*, 1999–2049. [[CrossRef](#)]
41. Muñoz-Sabater, J.; Dutra, E.; Agustí-Panareda, A.; Albergel, C.; Arduini, G.; Balsamo, G.; Boussetta, S.; Choulga, M.; Harrigan, S.; Hersbach, H.; et al. ERA5-Land: A State-of-the-Art Global Reanalysis Dataset for Land Applications. *Earth Syst. Sci. Data* **2021**, *13*, 4349–4383. [[CrossRef](#)]
42. Jiang, Y.; Yang, K.; Qi, Y.; Zhou, X.; He, J.; Lu, H.; Li, X.; Chen, Y.; Li, X.; Zhou, B.; et al. TPhIPr: A Long-Term (1979–2020) High-Accuracy Precipitation Dataset (1/30°, Daily) for the Third Pole Region Based on High-Resolution Atmospheric Modeling and Dense Observations. *Earth Syst. Sci. Data* **2023**, *15*, 621–638. [[CrossRef](#)]
43. Zhou, X.; Yang, K.; Ouyang, L.; Wang, Y.; Jiang, Y.; Li, X.; Chen, D.; Prein, A. Added value of kilometer-scale modeling over the third pole region: A CORDEX-CPTP pilot study. *Clim. Dyn.* **2021**, *57*, 1673–1687. [[CrossRef](#)]
44. Yang, K.; Chen, Y.; Lazhu, Zhan, C.; Ling, X.; Zhou, X.; Jiang, Y.; Yao, X.; Lu, H.; Ma, X.; et al. Cross-Sectional Rainfall Observation on the Central-Western Tibetan Plateau in the Warm Season: System Design and Preliminary Results. *Sci. China Earth Sci.* **2023**, *66*, 1015–1030. [[CrossRef](#)]
45. Dorigo, W.; Preimesberger, W.; Reimer, C.; Van der Schalie, R.; Pasik, A.; De Jeu, R.; Paulik, C. Soil Moisture Gridded Data from 1978 to Present, v202212.1.0. Copernicus Climate Change Service (C3S) Climate Data Store (CDS). 2019. Available online: <https://cds.climate.copernicus.eu/cdsapp#!/dataset/satellite-soil-moisture?tab=overview> (accessed on 31 October 2023).
46. Wang, L.; Han, S.; Tian, F.; Li, K.; Li, Y.; Tudaji, M.; Cao, X.; Nan, Y.; Cui, T.; Zheng, X.; et al. The Evaporation on the Tibetan Plateau Stops Increasing in the Recent Two Decades. *J. Geophys. Res.* **2022**, *127*, e2022JD037377. [[CrossRef](#)]
47. Wang, L.; Tian, F.; Han, S.; Cui, T.; Meng, X.; Hu, H. Determination of the Asymmetric Parameter in Complementary Relations of Evaporation in Alpine Grasslands of the Tibetan Plateau. *J. Hydrol.* **2022**, *605*, 127306. [[CrossRef](#)]
48. Rajeevan, M.; Gadgil, S.; Bhate, J. Active and Break Spells of the Indian Summer Monsoon. *J. Earth Syst. Sci.* **2010**, *119*, 229–247. [[CrossRef](#)]
49. Wang, B.; Fan, Z. Choice of South Asian Summer Monsoon Indices. *Bull. Am. Meteorol. Soc.* **1999**, *80*, 629–638. [[CrossRef](#)]
50. Wang, B.; Wu, R.; Lau, K.-M. Interannual Variability of the Asian Summer Monsoon: Contrasts between the Indian and the Western North Pacific–East Asian Monsoons. *J. Clim.* **2001**, *14*, 4073–4090. [[CrossRef](#)]
51. Reid, K.J.; King, A.D.; Lane, T.P.; Short, E. The Sensitivity of Atmospheric River Identification to Integrated Water Vapor Transport Threshold, Resolution, and Regriding Method. *JGR Atmos.* **2020**, *125*, e2020JD032897. [[CrossRef](#)]
52. Sousa, P.M.; Ramos, A.M.; Raible, C.C.; Messmer, M.; Tomé, R.; Pinto, J.G.; Trigo, R.M. North Atlantic Integrated Water Vapor Transport—From 850 to 2100 CE: Impacts on Western European Rainfall. *J. Clim.* **2020**, *33*, 263–279. [[CrossRef](#)]
53. Wan, G.; Yang, M.; Liu, Z.; Wang, X.; Liang, X. The Precipitation Variations in the Qinghai-Xizang (Tibetan) Plateau during 1961–2015. *Atmosphere* **2017**, *8*, 80. [[CrossRef](#)]
54. Sun, C.; Xu, X.; Zhao, T.; Yao, T.; Zhang, D.; Wang, N.; Ma, Y.; Ma, W.; Chen, B.; Zhang, S.; et al. Distinct Impacts of Vapor Transport from the Tropical Oceans on the Regional Glacier Retreat over the Qinghai-Tibet Plateau. *Sci. Total Environ.* **2022**, *823*, 153545. [[CrossRef](#)]
55. Liu, T.; Chen, J.; Yang, K.; Deng, L.; Guo, Z. Impacts of the Indian Summer Monsoon on the southern boundary water vapor transport and precipitation over the Tibetan Plateau. *Atmosphere* **2023**, *14*, 20. [[CrossRef](#)]
56. Sun, Y.; Gong, Y. Characteristics of abnormal changes of precipitation over the Tibetan Plateau and atmospheric circulation under the influence of Indian summer monsoon. *J. Chengdu Univ. Inf. Technol.* **2019**, *34*, 411–419. [[CrossRef](#)]

57. Tang, Y.; Dan, J.; Zhang, M.; Jiang, H.; Gao, Y. Recycling and Transport of Evapotranspiration over the Tibetan Plateau: Detected by a Water Vapour Tracer Method Embedded in Regional Climate Model. *Int. J. Clim.* **2023**, *43*, 7899–7914. [[CrossRef](#)]
58. Wang, Z.; Wu, R.; Huang, G. Low-frequency Snow Changes over the Tibetan Plateau. *Int. J. Clim.* **2018**, *38*, 949–963. [[CrossRef](#)]
59. Du, J.; Zhou, K.; Ci, W. Spatial and temporal variations of surface soil freezing days in Chang Tang Natural Reserve of Tibet during 1981–2018. *Chin. J. Ecol.* **2020**, *39*, 1121–1129. [[CrossRef](#)]
60. Liu, W.; Wen, J.; Chen, J.; Wang, Z.; Lu, C.; Wu, Y.; Jiang, Y. Characteristic Analysis of the Spatio-temporal Distribution of Key Variables during the Soil Freeze-thaw Process over the Qinghai-Xizang Plateau. *Plateau Meteorol.* **2022**, *41*, 11–23. [[CrossRef](#)]
61. Yang, S.; Liu, Z.; Yan, Y.; Ye, Z. Preliminary study on soil humidity and its relationships with soil temperature and air temperature in snow melting season. *Arid. Zone Res.* **2008**, *25*, 642–646. [[CrossRef](#)]
62. Williams, C.J.; McNamara, J.P.; Chandler, D.G. Controls on the Temporal and Spatial Variability of Soil Moisture in a Mountainous Landscape: The Signature of Snow and Complex Terrain. *Hydrol. Earth Syst. Sci.* **2009**, *13*, 1325–1336. [[CrossRef](#)]
63. Zhang, Y.; Ohata, T.; Kadota, T. Land-surface hydrological processes in the permafrost region of the eastern Tibetan Plateau. *J. Hydrol.* **2003**, *283*, 41–56. [[CrossRef](#)]
64. Yao, T.; Thompson, L.; Yang, W.; Yu, W.; Gao, Y.; Guo, X.; Yang, X.; Duan, K.; Zhao, H.; Xu, B.; et al. Different Glacier Status with Atmospheric Circulations in Tibetan Plateau and Surroundings. *Nat. Clim. Chang.* **2012**, *2*, 663–667. [[CrossRef](#)]
65. Yao, T.; Pu, J.; Lu, A.; Wang, Y.; Yu, W. Recent Glacial Retreat and Its Impact on Hydrological Processes on the Tibetan Plateau, China, and Surrounding Regions. *Arct. Antarct. Alp. Res.* **2007**, *39*, 642–650. [[CrossRef](#)]
66. Paudyal, R.; Kang, S.; Huang, J.; Tripathee, L.; Zhang, Q.; Li, X.; Guo, J.; Sun, S.; He, X.; Sillanpää, M. Insights into Mercury Deposition and Spatiotemporal Variation in the Glacier and Melt Water from the Central Tibetan Plateau. *Sci. Total Environ.* **2017**, *599*, 2046–2053. [[CrossRef](#)]
67. Su, F.; Zhang, Y.; Tang, Q.; Ding, J.; He, L.; Tang, Y.; Liu, X.; Liu, X.; Xu, X.; Sang, Y.; et al. Streamflow change on the Qinghai-Tibet Plateau and its impacts. *Chin. Sci. Bull.* **2019**, *64*, 2807–2821. [[CrossRef](#)]
68. Yang, K.; Ye, B.; Zhou, D.; Wu, B.; Foken, T.; Qin, J.; Zhou, Z. Response of hydrological cycle to recent climate changes in the Tibetan Plateau. *Clim. Chang.* **2011**, *109*, 517–534. [[CrossRef](#)]
69. Cheng, S.; Guan, X.; Huang, J.; Ji, F.; Guo, R. Long-term trend and variability of soil moisture over East Asia. *J. Geophys. Res.-Atmos.* **2015**, *120*, 8658–8670. [[CrossRef](#)]
70. Tang, Z.; Wang, J.; Li, H.; Yan, L. Spatiotemporal changes of snow cover over the Tibetan plateau based on cloud-removed moderate resolution imaging spectroradiometer fractional snow cover product from 2001 to 2011. *J. Appl. Remote Sens.* **2013**, *7*, 073582. [[CrossRef](#)]
71. Xu, W.; Ma, H.; Wu, D.; Yuan, W. Assessment of the daily cloud-free MODIS snow-cover product for monitoring the snow-cover phenology over the Qinghai-Tibetan Plateau. *Remote S.* **2017**, *9*, 585. [[CrossRef](#)]
72. Wang, G.; Dolman, A.J.; Blender, R.; Fraedrich, K. Fluctuation Regimes of Soil Moisture in ERA-40 Re-Analysis Data. *Theor. Appl. Clim.* **2010**, *99*, 1–8. [[CrossRef](#)]
73. Davarzani, H.; Smits, K.; Tolene, R.M.; Illangasekare, T. Study of the effect of wind speed on evaporation from soil through integrated modeling of the atmospheric boundary layer and shallow subsurface. *Water Resour. Res.* **2014**, *50*, 661–680. [[CrossRef](#)]
74. Dorigo, W.; Preimesberger, W.; Reimer, C.; Van der Schalie, R.; Pasik, A.; De Jeu, R.; Paulik, C. Soil Moisture Gridded Data from 1978 to Present, v201912.1.0. Copernicus Climate Change Service (C3S) Climate Data Store (CDS). 2019. Available online: <https://cds.climate.copernicus.eu/cdsapp#!/dataset/satellite-soil-moisture?tab=overview> (accessed on 31 October 2023).
75. Dorigo, W.; Preimesberger, W.; Reimer, C.; Van der Schalie, R.; Pasik, A.; De Jeu, R.; Paulik, C. Soil Moisture Gridded Data from 1978 to Present, v202012.0.0. Copernicus Climate Change Service (C3S) Climate Data Store (CDS). 2019. Available online: <https://cds.climate.copernicus.eu/cdsapp#!/dataset/satellite-soil-moisture?tab=overview> (accessed on 31 October 2023).
76. Owe, M.; De Jeu, R.; Holmes, T. Multisensor historical climatology of satellite-derived global land surface moisture. *J. Geophys. Res.* **2008**, *113*, 2007JF000769. [[CrossRef](#)]
77. Gruber, A.; De Lannoy, G.; Albergel, C.; Al-Yaari, A.; Brocca, L.; Calvet, J.-C.; Colliander, A.; Cosh, M.; Crow, W.; Dorigo, W.; et al. Validation Practices for Satellite Soil Moisture Retrievals: What Are (the) Errors? *Remote Sens. Environ.* **2020**, *244*, 111806. [[CrossRef](#)]
78. Wang, Z.; Liu, Y.; Yang, J.; Liu, Z. Multi-scale Evaluation and Validation of Soil Moisture Products of FY-3B/3C and CLDAS: A Case Study in Naqu Region of the Qinghai-Tibet Plateau. *Chin. J. Agrometeorol.* **2021**, *42*, 788–804. [[CrossRef](#)]
79. Wang, Y.; Yang, Y.; Liu, C.; Shi, C. Analysis on the applicability of Fengyun-3 satellite microwave remote sensing soil moisture products in Shandong. *Chin. J. Agrometeorol.* **2021**, *42*, 318. [[CrossRef](#)]

Disclaimer/Publisher's Note: The statements, opinions and data contained in all publications are solely those of the individual author(s) and contributor(s) and not of MDPI and/or the editor(s). MDPI and/or the editor(s) disclaim responsibility for any injury to people or property resulting from any ideas, methods, instructions or products referred to in the content.